Smart Gold-Polymer Nanostructures As Promising Drug Nanocarriers For Dual-Imaging Modality And Synergistic Chemo-Photothermal Therapy in Breast Cancer Cells

Mehdi Azizi
Tabriz University of Medical Sciences
Asrin Pakravan
Azarbaijan University of Tarbiat Moallem: Azarbaijan Shahid Madani University
Hadi Valizadeh
Tabriz University of Medical Sciences
Reza Rahbarghazi
Tabriz University of Medical Sciences
Hassan Dianat-Moghadam
Tabriz University of Medical Sciences
Farhad Bani
Tabriz University of Medical Sciences
Houman Kahroba
Maastricht University Hospital: Maastricht Universitair Medisch Centrum+
Roya Salehi (salehiro@tbzmed.ac.ir)
Tabriz University of Medical Sciences
Mohammad Mehrmohammadi
Wayne State University

Research

Keywords: Gold-Polymer Nanostructures, Theranostic, Chemo-Photothermal Therapy, Dual-Imaging Modality, Tumoricidal Effects

Posted Date: October 27th, 2021

DOI: https://doi.org/10.21203/rs.3.rs-982173/v1

Abstract

To improve the efficacy of cancer therapeutics, highly sensitive imaging with precise accuracy is mandatory for timely diagnosis and selection of strategic approaches. Despite recent advances in technologies associated with tumor imaging, the application of conventional single-mode imaging is the subject of debate. Herein, two types of pH-responsive gold-polymer nanostructures, GNSts and GNRs, containing CD and MTX, GNSts-MTX@CD-Pol and GNRs-MTX@CD-Pol were designed. Dual-imaging modalities (fluorescence and CT imaging) and synergistic chemo-photothermal therapy were examined in human breast cancer MDA-MB 231 cells.

MTT assay showed NIR irradiation of cells pre-treated with synthesized nanoparticles promoted tumoricidal synergy via the reduction of survival rate after 48 hours in comparison with the control group ($p<0.05$), indicating a high absorption coefficient in the NIR area and efficient heat production rate. Flow cytometry, real-time PCR and western blot, analyses indicated an apoptotic cell death induced by the up-regulation of Caspases 3, 6, 7, 8, and 9, Bax, and Annexin-V, confirming the activation of intrinsic and extrinsic apoptosis pathways inside the host cells. The elevation of p27 and p53 in line with the increase of cell percent at the subG1 phase showed apoptotic changes and inhibition of dynamic cell growth compared to the non-treated cells ($p<0.05$). Evident fluorescence intensity at lower pH values (6.3) showed pH-dependent activity of nanoparticles internalized by surface folate receptor. Of note, we showed strong capability for CT imaging in cells incubated with GNSts-MTX@CD-Pol and GNRs-MTX@CD-Pol.

Taken together, all data show that gold-polymer nanostructures have considerable capability in theranostic applications like simultaneous diagnostic imaging and therapy.

Introduction

Cancer is one of the critical health problem and the second main reason of death globally [1]. For many years, a “one size fits all” model has been postulated for chemotherapy that is applicable for all cancer types. In the last decades, radiotherapy and chemotherapy have been widely in medical oncology. The efficiency of chemotherapy is closely associated with the biodistribution and delivery of drugs to the tumor stroma. However, the existence of chemo-resistant mechanisms attributes to drug resistance and cell metastasis to the remote sites [2–4]. Despite recent development in our knowledge about cancer biology, many cancer cases are diagnosed in the end stages because of the poor sensitivity and specificity of conventional detection systems, leading to a diminished survival rate [5]. As a correlate, nano-carriers with each passive or active targeting abilities have been developed for the early-stage detection and therapy of multiple cancer types. It was suggested that these nanocarriers would be eligible to rise the half-lives of therapeutic agents in the circulation system and accelerate passive distribution into the tumor niche via EPR mechanisms [6].

Nowadays, the paradigm in cancer cases and therapy has been changes from classical from the conventional therapeutic look towards a personalized medicine using theranostic [7]. The word theranostic attributes to the integration of diagnostic and therapeutic strategies with the rationale of increased safety and efficacy in each cancer patient [8]. Compared to available monotherapyies, simultaneous application of chemotherapeutic agents with other medications such as radiation, genetic manipulation, and photothermal irradiation enables us to efficiently suppress tumor development and expansion [9–11]. Among them, tumoricidal properties of chemo-photothermal therapy have been proved in the clinical setting [12]. It is postulated that coupling photothermal irradiation with chemotherapy yields a synergistic effect in which the mild to moderate hyperthermia generate by outer stimulus (laser) promotes coagulation in tumor blood vessels, leading to reduced cell resistance against drugs. In this regard, NIR laser is touted as common stimuli for heat generation. The exposure of distinct nanostructures such as GNS-, Cu-based nanostructures, and carbon nanotubes to NIR-based PTT support a low-risk treatment [13–15]. Because of their biological inertness, superior optical properties, non-toxicity and biocompatibility, and chemically modifiable surface, GNSs pave a way for reliable multifunctional platforms for the development of cancer nanotheranostics [16–18]. GNSs have the potential to efficiently scatter or absorb light at a tunable resonance frequency, named as LSPR. The LSPR properties enriched contrast for a range of optical imaging modalities containing CT, PAT and multi-photon photoluminescence imaging [19]. Besides, these nanoparticles directly convert the light into heat after PTT. Non-covalent or covalent conjugation of therapeutic agents to the GNSs surface can intensify anti-cancer properties.

Previously, a new type of MTX-driven CD was synthesized by our research group for self-targeting, imaging, and therapy of cancer cells [20]. Herein, we developed a novel ultra pH-sensitive copolymer composed of poly (ethylene glycol)-b-poly [2 (diisopropylamino) ethyl methacrylate-co-2-aminoethyl methacrylate (AEMA)] copolymer, (PEG-b-(P DiPAEMA-co-AEMA) with atom transfer radical polymerization. Then, GNSts and GNRs were fabricated and conjugated with MTX, as targeting ligand a chemotherapy agent, (GNSs-MTX). GNSs, as a quencher, were conjugated with an imaging fluorochrome MTX-derivative carbon dots (MTX-CDs) via PEG-b-P (DiPAEMA-co-AEMA) copolymer to develop multifunctional GNS-MTX@CD-Pol NSs. Both pH-responsive and tumoricidal properties of GNSs-MTX@CD-Pol NSs were investigated in human MDA-MB 231 breast cancer cells in combination with their PTT effect.

Material And Methods

Materials

HAuCl4 (≥99.9%), RB, MTT, PI, MTX, PMDETA, DiPAEMA, AEMA, EDC/NHS, 2-bromo-2-methyl propanoyl bromide, MeO-PEG_{114}-OH, DMAP, TEA, CTAB, $NaBH_4$, PVP, (Mw=40000 g/mol) and CuBr were purchased from Sigma-Aldrich Co. CuBr was suspended for 12 hours with an excess of glacial acetic acid, filtered and washed with absolute ethyl alcohol followed by anhydrous ethyl ether. The purified CuBr was

vacuum dried at 80˚C for 48 hours and stored under nitrogen at 4˚C. Sodium citrate ($Na_3C_6H_5O_7$. $2H_2O$, >99%), $AgNO_3$, AA, HCl, NaCl, NaBr, Na_2S (55%), and BSA were purchased from Merck Co and used without further purification. Deionized water (resistance >18.2 MΩ) was used in all experiments. Other materials that are used in biological protocols including Penicillin-Streptomycin, FBS, Ribonuclease (RNase), Trypsin-EDTA, and RPMI were obtained from Gibco BRL Life Technologies. To assess apoptosis, we purchased an apoptosis kit (ApoFlowEx® FITC Kit) from Exbio Inc.

Apparatus and Characterization

The optical behavior of synthesized GNSs were analyzed with double beam PC 1601 UV–Vis (SHIMADZU, Kyoto, Japan) spectrophotometer. TEM imaging [(TEM; LEO 906 TEM (Germany, Zeiss)] was performed at 100Kv acceleration voltages to investigate GNSs particle size, morphology. DLS and zeta potential (ζ) (DLS; Nano-ZS, Malvern Instruments (Malvern, UK) were utilized to measure GNSs particle size, and zeta potential values. ^1H NMR spectra were recorded on an FT-NMR Bruker spectrometer (Bruker, Ettlingen, Germany) with an operating frequency of 400 MHz at 25°C. FT-IR spectra were recorded on Bruker (Tensor 27) IR spectrophotometer instrument. Other analyses such as ICP-MS (Elan 6100DRC-e, Perkin-Elmer, Waltham, MA, USA), were applied for the evaluation of G ion concentration and quantification of GNSs uptake by MDA-MB 231 cells. GPC analysis was achieved with Shimadzu LC20A instrument using Waters Ultra-hydragel linear column (exclusion limit 0.2 to 80 KDa) and 0.1 M NaNO3 in water as mobile phase with the flow rate of 0.9 ml/min, the temperature of 35˚C.

Synthesis of GNRs

GNRs were synthesized by using the seedless growth method [21]. In short, the process is associated with the formation of GNRs based on the reduction rate of the gold ions in the growth solution. The pH of the growth solution was set to an acidic condition and sodium borohydride was used as a substitute of a seed solution for concurrent seed configuration and GNRs growth.

Decoration of GNRs with BSA

About 0.5 and 5 mg/ml BSA was dissolved in the deionized water and pH was adjusted to 7 and 12, respectively. Then, GNRs solution was added BSA solution (5 mg/ml; 1:3 rates, respectively) under sonication. Sonication was continued for 40 minutes. Afterward, the solution was centrifuged at 10000 rpm for 10 minutes to exclude excess BSA. Finally, centrifuged GNRs were spread in BSA solution (0.5 mg/ml; 1:3 rates, respectively) and shacked for 24 hours at room temperature (RT). Thereafter, the reaction was ended by eliminating the additional BSA via centrifugation at 10,000 rpm for 10 minutes and re-suspended the precipitate in ultrapure deionized water [22].

Synthesis of GNSts

GNSts were synthesized using a seed-mediated growth two-step technique described previously [23]. The GNSPhs with an approximate size of13 nm were synthesized with the Turkevich method. The procedure was followed by the surfactant-free method [24].

Synthesis of PEG_{114}-b-P (DiPAEMA-co-AEMA)

PEG macroinitiator (MeO-PEG_{114}-Br) were obtained just as the method described below. To activate MeO-PEG_{114}-OH, we dissolved 0.92 g of DMAP in dry THF. After the addition of 0.7 ml of TEA to the solution, the components were added to a three-necked balloon under dry argon atmosphere flow. Of note, 12.5 g of MeO-PEG-OH was dissolved in 50 ml of dry THF and added dropwise to the three-necked balloon. The temperature of the balloon was set at zero degrees by an ice bath. After this step, 1.54 ml of 2-bromo-isobutyryl bromide dissolved in 10 ml of dry THF and slowly added to the three-necked balloon using a syringe. After adding all the components, the color of the solution transformed to pale yellow. The above solution was stirred under argon flow at 280 rpm for 18 hours until the reaction was completed. Then, the obtained product was filtered and the precipitate was placed at RT for complete drying [25]. Final polymer were synthesized by the ATRP method. To this end, 1.71 g DiPAEMA (8 mmol), 100 mg AMA (0.6 mmol), 21 µl PMDETA (0.1 mmol), and 0.5 g MeO-PEG_{114}-Br (0.1 mmol) were dissolved in solvent mixed (2-propanol (2 ml) and DMF (2 ml)) and poured in a polymerization tube. Dissolved oxygen was removed by three cycles of freeze-pump-thaw. Then 14.4 mg CuBr (0.1 mmol) was added into the reaction tube under a nitrogen flow, and the tube was sealed in vacuo. The polymerization was done at 40°C for 12 hours. After the completion of the polymerization step, the reaction mixture was diluted with 10 ml THF and dialyzed to remove the catalyst. The solvent was eliminated by a rotary evaporator (Heidolph, Germany). The product was dialyzed in distilled water and lyophilized to obtain a white powder.

Synthesis of PEG_{114}-b-P (DiPAMA-co-AEMA-r-CD)

CDs were activated by EDC/NHS for 48 hours. After then, 50 mg PEG_{114}-b-P (DiPAMA-co-AEMA) dissolved in 2 ml of anhydrous DMF followed by the addition of an activated CD, and stirred at RT for two consecutive days. The synthesized polymer were purified by dialyze bag to eliminate the free CDs, lyophilized and stored at -20°C.

MTX loading on GNSs and self-assemble of GNSs-MTX@CD-Pol

For drug loading, 5 µl (25 mM) MTX was added to 500 µl of 100 ppm GNSs and stirred overnight at RT. Unbound MTX was removed from the mixture by centrifuging at 10,000 rpm for 10 minutes. The procedure was followed by washing with 10 mM phosphate buffer (pH=7.2) three times [26]. Next, 150 µl of PEG-b-P(DiPAEMA-co-AEMA-r-CD) (1 mg/ml) dissolved in DMF was added to 8500 µl GNSs-MTX solution (50 ppm, in DMF) under vigorous stirring. Then, 0.3 ml of Tris-HCl was added dropwise at RT. Thereafter, 20 µl dodecanethiol solution (20 µl in 2 mL of DMF) was added to the solution and stirred for 1 hour. Another 3 mL of Tris-HCl was added dropwise to the mixture. The organic solvent was eliminated by dialysis using PBS for 24 hours. Lastly, the solution in the dialysis bag was centrifuged at 10000 rpm for 10 minutes. The copolymer-decorated GNSs were re-dispersed in 1 ml of PBS (pH= 7.4) [27].

Photothermal procedure

To test whether GNSs and GNSs-MTX@CD-Pol can exhibit efficient photothermal effects, 50 µg/ml GNSs and GNSs-MTX@CD-Pol were dissolved in PBS. Then, 200 µl of each solution was poured into per well of 96-well plates. The plates were exposed to continuous-wave NIR laser Diode (λ = 808 nm; 2.5 W, Model: PSU-III-LED, Changchun new institute, China) at a power density of 0.7 W/cm^{-2} at different time points including 2, 4, 6, 8, and 10 minutes. The PBS temperature was monitored throughout irradiation using a digital thermocouple (LCD K-Type Digital Thermometer, Model: TM-902C w Thermocouple Wire, Shenzhen, China) immersed directly into suspensions. Temperature rises of the suspensions were recorded as a function of the irradiation time, and initial points for all of the nanostructure were recorded as t = 0.

Cell viability assay

The tumoricidal effects of GNSs and GNSs-MTX@CD-Pol were assessed using conventional MTT assay. For this purpose, human breast cancer MDA-MB 231 cells were seeded in 96-well culture plates at an initial density of 1×10^4 cells per well. Cells were suspended in RPMI1640 medium supplemented with 10% FBS and 1% Penicillin/Streptomycin and kept at standard culture condition (37°C with 5% CO_2). Upon reaching 70% confluence, cells were treated with different concentrations (ranging from 0 to 100 µg/ml) of GNSs and GNSs-MTX@CD-Pol for 24 hours. Untreated cells were considered as the control group. After completion of incubation time, the culture medium was discarded and cells were washed two times with PBS. Then, 200 µl MTT solution (5 mg/ml) was added to each well, and plates were retained at 37˚C for 4 hours. After discarding the supernatant, 200 µl of DMSO was added to dissolve formazan crystals. Lastly, the optical densities of every well were assessed by an ELISA plate reader (Awareness Technology, Palm City, FL, USA) at 570 nm with a reference wavelength of 630 nm. All measurements were performed in triplicate and statistical analysis was carried out using OriginPro software.

Photothermal effects on cells pre-treated with GNSs and GNSs-MTX@CD-Pol

To this end, MDA-MB 231 cells were cultured in 96-well plates and pretreated with 50 µg/ml GNSs and GNSs-MTX@CD-Pol for 3 hours. Thereafter, the supernatant was discarded and cells were washed three times with PBS to eliminate the free formulations. Cells were then exposed to NIR light at recommended doses. In this study, irradiated cells without GNSs treatment were considered as a positive control group. The cytotoxicity of each group was measured by MTT assay.

In vitro cell uptake of GNSs and GNSs-MTX@CD-Pol

ICP-MS analysis of cell uptake

To this end, $5\cdot10^5$ MDA-MB 231 cells were seeded per well of 6-well plates (24 h) and incubated with GNSs and GNSs-MTX@CD-Pol for 4 hours. Following PBS washes, cells were trypsinized, counted, and

digested in concentrated HNO_3 for 1 hour at 90–100°C. The suspension was recovered and diluted in 1% HCl, and the Au extent was obtained by ICP-MS as previously described [28, 29].

Flow cytometric analysis of cell uptake

Quantitative analysis of GNSs and GNSs-MTX@CD-Pol uptake was done using flow cytometry. In brief, 1 ml of nanoformulations mixed with 200 µl of RhoB in PBS and stirred overnight at RT in dark conditions. Afterward, RhoB-loaded GNSs and GNSs-MTX@CD-Pol were separated using Amicon® Ultra Centrifugal filters with molecular Cut off of 50KDa. To eliminate unloaded RhoB, the precipitates were washed several times with PBS. For the flow cytometry analysis, 5×10^5 cells/well MDA-MB 231 cells were seeded onto coverslips in 6-well culture plates and incubated for 24 hours at 37°C. 2 ml culture medium containing RhoB-labeled nanostructures at a concentration of IC_{50} was poured into each well and cell incubated with 1 and 4 hours. Non-treated cells was considered as a negative control. Finally, cells were collected and investigated using a BD® FACSCalibur flow cytometer (USA).

Dual-modality CT and fluorescence imaging of cancer cells

For this purpose, MDA-MB 231 cells was seeded onto culture dishes at a density of 2×10^6 cells per plate and cultured for 24 h at 37°C and 5% CO_2. Then cells were incubated for 3 hours in a culture medium containing 50 µg/ml of GNSts-MTX@CD-Pol and GNRs-MTX@CD-Pol, following PBS wash, dual-modality CT and fluorescence imaging were performed. CT images were captured by a CT imaging system with 50 kVp, 0.800 mA, and fluorescence imaging was done using Plan Apo apochromatic objectives (Nikon, Tokyo, Japan) and a fluorescence microscope (Olympus microscope Bh2-FCA, Japan). The best fluorescence excitation was detected while mirror cube units adjusted for 480–510 and 510–550 nm.

Cell cycle analysis

Following 3-hour incubation of MDA-MB 231 cells with 50 µg/ml of GNSs and GNSs-MTX@CD-Pol and exposure to laser irradiation, cells were kept for the next 48 hours, collected for cell cycle analysis. In short, cells were fixed in 70% ice-cold ethanol, incubated with ribonuclease solution, stained with PI solution, and analyzed with FACSCalibur flow cytometer [30].

Flow cytometric analysis of apoptosis

Following 3-hour incubation of MDA-MB 231 cells with 50 µg/ml GNSs and GNSs-MTX@CD-Pol and exposure to laser irradiation, cells were kept for the next 48 hours. Then cells were collected using Trypsin-EDTA, washed with PBS, and incubated in 1X Annexin binding buffer. For cell staining, suspensions were incubated in a binding buffer containing 5 µl Annexin-V and 5 µL PI according to the manufacturer's instruction. Using a flow cytometry system, the percent of cells with early and late apoptotic changes was calculated.

Real-time PCR (RT-qPCR) analysis

The expression of different genes related to apoptosis, such as CASPASE-3, 6, 7, 8, 9, 10, 12, Bax, and Bcl-2, was monitored in the treated cells (with 50 µg/ml GNSs and GNSs-MTX@CD-Pol and exposure to laser

irradiation) using real-time PCR analysis. Total RNA content was extracted from different groups using the TRIzol® method [31]. The integrity and content of RNA were determined by NanoDrop Spectrophotometer. The extracted RNA was reverse-transcribed into cDNA by a reverse transcription Kit (Bioneer, Korea). RT-qPCR was achieved by QuantiTect SYRB Green dye (TaKaRa, Japan) and Corbett Rotor-Gene™ 6000 HRM system. RT-qPCR primer sequences were outlined in Table 1 according to our previously published data [31, 32]. The expression amount of each gene were investigated by Pfafl technique with normalization to the housekeeping gene, Glyceraldehyde-3-Phosphate Dehydrogenase (GAPDH).

Table 1
Primer list

Gene	Forward primer	Reverse primer	Tm (˚C)
CASPASE-3	GAAATTGTGGAATTGATGCGTGA	CTACAACGATCCCCTCTGAAAAA	60
CASPASE-6	ATGGCGAAGGCAATCACATTT	GTGCTGGTTTCCCCGACAT	60
CASPASE-7	AGGGACCGAGCTTGATGATG	CACTGGGATCTTGTATCGAGGA	60
CASPASE-8	GATCAAGCCCCACGATGAC	CCTGTCCATCAGTGCCATAG	60
CASPASE-9	CTTCGTTTCTGCGAACTAACAGG	GCACCACTGGGGTAAGGTTT	60
CASPASE-10	AGAAACCTGCTCTACGAACTGT	GGGAAGCGAGTCTTTCAGAAG	60
CASPASE-12	TGTTACAAAGGCTCATGTGGAAA	GGGTCAGTATATTTGGGGTCTCA	60
Bax	TTCTGACGGCAACTTCAACT	CAGCCCATGATGGTTCTGAT	60
Bcl-2	GGGAATCGATCTGGAAATCCTC	GGCAACGATCCCATCAATCT	60
GAPDH	ACAACTTTGGTATCGTGGAAGG	GCCATCACGCCACAGTTTC	60

Western blotting

In line with gene expression analysis, protein levels of Caspase 3, 9, P53, P27, Bax, and Bcl-2 were investigated using western blotting. After completion of the experimental procedure, MDA-MB 231 cells were lysed using protein lysis buffer (25 mM HEPES, 1% Triton X-100, 2 mM EDTA, 0.1 mM NaCl, 25 mM NaF, and 1 mM Sodium Orthovanadate) enriched with protease cocktail inhibitor (Roche). Samples were kept on ice for 30 minutes and then were vortexed. Cell lysates were centrifuged at 12000 g for 20 minutes. The supernatants were collected and the contents were determined using Picodrop (Cambridge, UK). An equal amount of protein (~100 µg) was separated using 10% SDS-PAGE and transferred onto the PVDF membrane. Skim milk (5%) was used to block non-specific binding sites and membranes were incubated with antibodies against Caspase 3, 9, P53, P27, Bax, and Bcl-2 (all purchased from Santa Cruz Biotechnology Inc., USA) for 1 hour at RT. Immuno-reactive bands were visualized using ECL reagent (BioRad) and X-ray films. The density of each band was determined using Image J software (version 1.4; NIH).

Result And Discussion

Synthesis and characterization of pH-responsive and self-assembled GNSs probes

Here, we constructed the multifunctional GNSs (GNRs and GNSts) and were coated with pH-sensitive PEG-b-P (DiPAEMA-co-AEMA-r-CD) (Pol-CD@GNSs-MTX). The GNRs and GNSts were synthesized using seed-mediated and galvanic replacement methods, respectively. TEM imaging revealed an average size of 32 ± 5.2 and 43.2 ± 8.2 nm for GNRs and GNSts, respectively (Figure 1). According to LSPR spectroscopy, maximum absorption peaks were in the wavelength of 807 and 768 nm before polymer coating, respectively (**Figure S1**). The hydrodynamic diameter of the as-prepared GNRs and GNSts was about 87 and 116 nm. Of note, zeta potential values reached -32.5 and 24.3 mV in an aqueous solution (Table 2 and **Figure S2-S3**). The dodecanethiol and MTX were used to cover GNRs and GNSts making the GNSs core hydrophobic to triggering the self-assembly of the copolymer onto the GNSs-MTX as targeting and drug agent (as an analog of folic acid to folate receptor targeting), respectively. Based on our data, the amount of MTX in MTX-GNRs and MTX-GNSts were 0.76 and 0.93 $\mu g/mL^{-1}$.

Table 2
Hydrodynamic diameter, PDI, and Zeta potential of GNSs and Pol-CD@GNSs-MTX.

Structures	Size (nm)	PDI	Zeta potential (mV)
GNRs (BSA)	87.31	0.335	-32.5
GNRs -MTX@CD-Pol	181.1	0.554	14.7
GNSts	116	0.493	24.3
GNSts -MTX@CD-Pol	143	0.4	16.9

In the next step, we synthesized a pH-responsive copolymer using the ATRP method [27]. The synthesis root of MeO-PEG114-Br and PEG_{114}-b-P (DiPAEMA-co-AEMA) is shown schematically in **Figures S4a** and **2a**, respectively. The chemical structure of the MeO-PEG114-Br and P PEG_{114}-b-P (DiPAEMA-co-AEMA) was analyzed by ^{1}HNMR using $CDCl_3$ as the solvent (**Figures S4b and 2b**) and FTIR spectroscopy (**Figures S4c** and **S5)**. The characteristic peaks of MeO-PEG114-Br moiety were observed at δ = 3.6-3.8 ppm (t, 4H, (-OCH_2-CH_2-O) and δ = 1.97ppm (s, 6H, C(CH_3)Br. The chemical shifts of the DIPAEMA segment appeared at δ = 4.3 ppm (t, 2H, O=C-O(CH_2)), δ = 3.5 ppm (t, 2H, CH_2-N($CH(CH_3)_2$), δ = 1.79 ppm (s, 2H, N($CH(CH_3)_2$) and δ = 3.38 ppm (s, 12H, N($CH(CH_3)_2)_2$). The characteristic peaks related to the AEMA moiety of the copolymer were observed at δ = 3.82 ppm (t, 2H, CH_2-NH_2) and δ = 5.26 ppm (2H, CH_2-NH_2). Finally, peaks that appeared at 1.4 and 1.6 ppm were related to polymer backbone protons. Synthesized PEG114-b-P(DiPAEMA-co-AEMA) was also characterized by FTIR spectroscopy (**Figure S5**). A signal at 1112 cm^{-1} was related to the stretching vibration of the eteric C-O-C parts of the copolymer. Moreover, the strong peaks at 2888 and 1350 cm^{-1} are associated to the aliphatic C-H stretching and

bending mode, respectively. The absorption band at 1736 cm^{-1} was related to the stretching vibration of esteric carbonyl (C = O) groups of copolymer. The peak that appeared at 3449 cm^{-1} correlated to the stretching vibration of N-H groups in AEMA. Molecular weights (Mn and Mw) and poly dispersity index (PDI) copolymer obtained by GPC was 9362 Daltons, 8429 Daltons, and 1.11, respectively (**Figure S6**). The predicted molecular weight obtained by ^{1}HNMR spectroscopy was around 9855 Daltons. This co-polymer was composed of PEG which functioned as a maintaining of colloidal dispersity of GNSs in aqueous solutions and hydrophobicity switchable block bear of TA. In the current study, DiPAEMA was employed to the hydrophobicity of the TA segment as well as adjusting of pKa value (6.2-6.4). To monitor the reversible pH-responsivity, an MTX-CD dye [20] was conjugated to the P(DiPAEMA-co-AEMA) copolymer as an imaging beacon, producing PEG-b P(DiPAEMA-co-AEMA-r-CD). It is thought that the TA groups were deprotonated and the segments became hydrophobic in the normal tissue conditions (pH 7.4). The MTX-CDs dyes were close to the GNSs, so their fluorescence was effectively quenched. In final self-assembled nanostructures, absorption bands of GNSs red-shift in the UV-Vis spectra (**Figure S1**). TEM images disclosed the core-shell structures of synthesized nano-assemblies with a nearly 5 nm thickness surrounding the GNSs cores (Figure 1). The hydrodynamic diameter and zeta potential of Pol-CD@GNRs-MTX and Pol-CD@GNSts-MTX were 181 nm, 14.7mV, and 143 nm, 16.9 mV, respectively (**Table. 2** and **Figure S1)**.

Biocompatibility and cellular uptake of Pol-CD@GNSs-MTX

To analyze the tumoricidal effect of GNSs and Pol-CD@GNSs-MTX on MDA-MB 231 cells and determine IC_{50} values, an MTT assay was performed (Figure 3). Data revealed dose-dependent activity of GNSs and Pol-CD@GNSs-MTX on cancer cells after 24 and 48 hours. The IC_{50} values of GNRs and GNSts-treated MDA-MB 231 cells were 50 and 100 µg/mL after 24 and 48 hours (Figure 3a-b). We noted that decoration of GNSs with polymer (Pol-CD@GNSs-MTX) reduced cytotoxic effects. It was estimated that more than 60% of cells were viable after exposure to 100 µg/mL Pol-CD@GNSs-MTX and this amount reached more than 80% at the concentration of 50 µg/mL (Figure 3d). In line with these data, 50 µg/mL Pol-CD@GNSs-MTX was selected for *in vitro* cell analyses. According to our data, PEG-b-P(DiPAMA-co-AEMA) copolymer did not exhibit significant cytotoxicity at concentrations up to 50 µg/mL (Figure 3c). In concentrations, more than 50 µg/mL, the survival rate of MDA-MB 231 cells was diminished in which in the group received 200 µg/mL PEG-b-P(DiPAMA-co-AEMA) near 50% of cells showed cytotoxicity.

Cell Uptake studies

To evaluate the potential role of MTX to target folate receptors and promote cellular uptake, quantitative uptake of Pol-CD@GNSs-MTX was evaluated in the MDA-MB 231 cells via flow cytometry (Figure 4a) and ICP-MS analyses (Figure 4b). According to Figure 4a, the mean fluorescence intensity (%) of Pol-CD@GNRs-MTX and Pol-CD@GNSts-MTX was significantly more compared to the Pol-CD@GNSts without MTX (P value<0.001), indicating the higher cellular uptake of MTX containing formulations due to targeting effect of MTX for folate receptor targeting. Mean fluorescent intensity results showed that 4-

hour incubation of cells with Pol-CD@GNRs-MTX and Pol-CD@GNSts-MTX led to higher cellular uptake compared to the matched groups incubated for 1 hour (P value<0.01). Also at 4-hour incubation, Pol-CD@GNSts showed higher cellular uptake compared to Pol-CD@GNRs.

Synergistic tumoricidal effect of PTT and Pol-CD@GNSs-MTX

To assess the synergistic tumoricidal effect of PTT and Pol-CD@GNSs-MTX, we measured the photothermal effect by monitoring the changes in temperature of the aqueous phase upon laser irradiation (808 nm, 0.7W/cm^2, for 2-10 minutes). The temperature was not altered in nanoparticle-free media in response to the irradiation (Figure 5a). By contrast, the existence of 50 µg/mL GNSs and Pol-CD@GNSs-MTX in the media culture medium temperature at a similar condition. This effect would be related to the photo-to-heat energy-converting effect of GNSs and Pol-CD@GNSs-MTX after exposure to the NIR laser. The amount of temperature increase was proportional to the GNSs and Pol-CD@GNSs-MTX concentration and irradiation time. Thus, it was notified that GNSs and Pol-CD@GNSs-MTX have the potential to be used as PTT agents in cancer therapy.

Encouraged by the above investigation, we evaluated the NIR laser-induced photothermal oncostatic properties in cancer cells pre-incubated with GNSs. For this purpose, MDA-MB 231 cells were treated with 50 µg/mL GNRSs and GNSts for 4 hours in dark conditions. Then, cells were exposed to irradiation for 10 minutes according to the above-mentioned protocol. Data showed that the viability of MDA-MB 231 cells decreased drastically and reached about 21 and 23% after treatment with GNRs/GNSts and laser irradiation compared to the non-treated control group (Figure 5b). This value was declined to 12 and 16% in Pol-CD@GNSts-MTX and Pol-CD@GNRs-MTX treated group respectively exposed to laser irradiation, indicating synergy of designed nanoparticles and PTT in the inhibition of cancer cells. In the group that received laser irradiation, slight but non-significant differences were found regarding cytotoxicity as compared to the control group.

Combination of Pol-CD@GNSs-MTX and PTT induced apoptosis and prohibited cell growth

The therapeutic property of GNSs and Pol-CD@GNSs-MTX were determined in MDA-MB 231 cells in the absence and presence of NIR laser using flow cytometric analysis of cell cycle (Figure 6a-b) and apoptosis (Figure 7). These methods are commonly used to determine DNA duplication in the cell cycle at phases G_1, S, and G_2/M. Compared to the non-treated control group, in groups that received laser irradiation and MTX alone, about 14 and 18% of the cells were observed in the subG1 phase, respectively. Treatment of cells with Pol-CD@GNSs-MTX alone showed 46% of cancer cells were at subG1 phase and this values reached 51% in the group received laser irradiation and GNSs (Figure 6a-b). The irradiation of cells pre-incubated with Pol-CD@GNSts-MTX and Pol-CD@GNRs-MTX led to the cycle arrest of 77% cells at the subG1 phase. The increase of cell number at the subG1 phase can be associated with apoptotic

cell death, leading to reduced cell entry to the G2/M and S phases [32]. In support of this claim, we noted that the percent of proliferating cells at the G2/M phase was diminished in groups that received the combination of laser irradiation and synthesized nanoparticles.

An Annexin-V/PI assay was done via flow cytometry to measure the percent of cells with early and late apoptotic changes (Figure 7). Data revealed the existence of apoptotic and necrotic changes in groups treated with laser irradiation, nanoparticles, or laser irradiation plus nanoparticles. In the group that received laser irradiation alone, we noted that the majority of cell death occurred due to necrosis reaching 12%. This value was about 21% in cells treated with MTX alone. Irradiation of cells pre-treated with GNRs and GNSts led to both apoptotic (52 versus 59%) and necrotic death (40 versus 48%), reaching, respectively. It seems that irradiation of cells pre-treated with Pol-CD@GNRs-MTX and Pol-CD@GNSs-MTX apoptosis is the hallmark of cell death in which about 91 and 92% of cells showed apoptosis, respectively. Commensurate with our data, late apoptotic changes were more evident cytotoxic effects in cells that received Pol-CD@GNSs-MTX and laser irradiation. The higher apoptotic percentage in Pol-CD@GNSs-MTX/L groups compared to GNSs/L groups that observed in cell cycle and Annexin-V test is related to their higher cell internalization (proved by flow cytometry and ICP-MS methods). Cell uptake showed a significant role in increasing photothermal efficiency. The amount of heat generation inside the cell is directly related to the number of nanoparticles adsorbed to the cell. This inside the cell destroys the cell.

Bax, Bcl2, and different Caspase subsets participate can regulate the apoptotic response [31]. To this end, we measured the expression and protein levels of pro- and anti-apoptotic factors using QRT-PCR analysis and western blotting, respectively. It was suggested that the expression of Caspase 8 is associated with stimulation of TNF receptor, showing the stimulation of extrinsic apoptotic response. In contrast, up-regulation of Caspase 9 is related to mitochondrial injury and can trigger an internal apoptosis signaling pathway [33]. In the next step, both Caspase 8 and 9 activate the common apoptosis pathway consisted of Caspase 3, 6, and 7 [31].

In general, we found that the exposure of MDA-MB 231 cells to Pol-CD@GNRs-MTX and Pol-CD@GNSts-MTX increased the expression of different pro-apoptotic genes such as Bax, Caspases 3, 7, 8, 9, 10, and 12 compared to the group received only MTX or laser irradiation alone, indicating higher tumoricidal effect of MTX in developed NPs ($p<0.05$) (Figure 8). These changes coincided with the reduction of anti-apoptotic effector Bcl-2 ($p<0.05$). These data were in accordance with flow cytometry analysis showing enhanced Annexin-V levels in these groups. Heat map analysis exhibited the expression apoptosis-related genes were control and laser irradiation (alone) groups were at the minimum levels, showing the lack of apoptotic response compared to other groups. Compared to MTX- and laser-treated cells, the exposure of MDA-MB 231 cells to Pol-CD@GNRs-MTX and Pol-CD@GNSts-MTX plus laser irradiation yielded maximum apoptotic changes with significant upregulation of Bax, Caspases 3, 7, 8, 9, 10, and 12 and down-regulation of Bcl-2 ($p<0.05$). These data showed that both intrinsic and extrinsic apoptosis signaling pathways were activated in cancer cells exposed to the combination of Pol-CD@GNRs-MTX and Pol-CD@GNSts-MTX plus laser groups.

Western blot analysis was done to analyze the executive apoptotic protein levels. The outcomes showed that the apoptotic process was initiated through the activation of Bax, Caspases 3, and 9 (Figure 9). Compared to the control group, the protein levels of Bax, Caspases 3, and 9 were increased in Pol-CD@GNSts-MTX/Laser, Pol-CD@GNRs-MTX/Laser groups (Figure 9). By contrast, these changes coincided with the suppression of anti-apoptotic protein Bcl2. Increased cleavage of Caspases 3 and 9 showed the activation of mechanisms related to proteolytic changes in different subcellular locations. In line with these changes, the increase of p53 and p27 and suppression of Bcl-2 showed the inhibition of the cell cycle and subsequent apoptotic changes [47]. A two-fold increase in p27 protein in comparison with the control can be related to cell cycle arrest following treated Pol-CD@GNRs-MTX/L and Pol-CD@GNSts-MTX/L which are in accordance with PI cell cycle analysis.

Cell imaging

Multimodal imaging can incorporate the benefits of all imaging modality [34]. In this study, multifunctional Pol-CD@GNSs-MTX could combine two modalities as follows; fluorescence and CT imaging. To determine the practicability of Pol-CD@GNSs-MTX for *in vitro* dual-modality imaging, fluorescence, and CT imaging was simultaneously conducted in the MDA-MB 231 cells pre-incubated with Pol-CD@GNSs-MTX (Figure 10). A fluorescent image was done in Pol-CD@GNSs-MTX treated cells at different pH values. Strong fluorescent intensity was observed at pH 5.2 and 6.3, while in higher values (pH 7.4) no detectable fluorescence signal was achieved, indicating the crucial importance of pH for the activation of Pol-CD@GNSs-MTX inside the host cells (Figure 10b). The existence of green fluorescence intensity in MDA-MB 231 cells after treatment with Pol-CD@GNSs-MTX can be related to a relatively acidic pH because of active glycolysis mechanisms inside these cells. It is suggested that the value of pH is about 7.4 in the normal tissues. Therefore, the TA groups of poly DiPAEMA segments were deprotonated and self-assemble into the hydrophobic cores of micelles, leading to the aggregation of structure and quenching of fluorescent signals because the MTX-CDs dyes were close to the GNSs, so their fluorescence was effectively quenched. At lower pH values (5.2 and 6.3), the protonation of TA groups of poly DiPAEMA, cause to micelle disassembly and an intense intensification in fluorescence emission because of the increase in CDs distance to the GNSs. These data were supported by the existence of prominent fluorescence activity in Pol-CD@GNSs-MTX-treated MDA-MB 231 cells at pH values of 6.3 and 7.4 (Figure 10a). In the meantime, the CT imaging of Pol-CD@GNSs-MTX displays similar trends to fluorescence imaging. As shown in Figure 10c, CT signal intensity resulted in brighter images (radioopacity). At adjusted pH (6), no significant difference was detected among the CT signals of Pol-CD@GNSs-MTX- and Pol-CD@GNRs-MTX-treated cells. Those results suggest that Pol-CD@GNSs-MTX have excessive prospective for concurrent CT and fluorescence imaging for cancer cells.

Conclusions

In summary, our data showed multifunctional activity of Pol-CD@GNSs-MTX and the synthesized nanoparticles can be touted as dual imaging and therapeutic agents in the tumor niche. It is suggested that the multifunctionality of Pol-CD@GNSs-MTX is based on the activity of GNSs and CDs. *In vitro*

experiments showed that Pol-CD@GNSs-MTX exhibited a strong X-ray attenuation for CT and fluorescence imaging. Moreover, we noted an increased tunable therapeutic efficacy of Pol-CD@GNSs-MTX upon laser irradiation. Pol-CD@GNSs-MTX induced apoptotic cell death in cancer cells exposed to NIR. We believe this multifunctional Pol-CD@GNSs-MTX will have excessive probability in theranostic applications like simultaneous diagnostic imaging and therapy.

Abbreviations

1-Ethyl-3-(3-dimethylaminopropyl) carbodiimide (EDC); 2-(di isopropyl amino) ethyl methacrylate (DiPAEMA); 2-aminoethyl methacrylate (AEMA); 3-(4,5-dimethylthiazol-2-yl)-2,5-diphenyl tetrazolium bromide (MTT); Ascorbic acid (AA); Atom transfer radical polymerization (ATRP); Bovine serum albumin (BSA); Carbon dots (CD); Cetyl trimethyl ammonium bromide (CTAB); Dimethyl aminopyridine (DMAP); Dynamic Light Scattering (DLS); Enhanced tumor penetration and retention (EPR); Fetal bovine serum (FBS); Gel permeation chromatography (GPC); Gold nanorods (GNRs); Gold nanospheres (GNSPhs); Gold nanostars (GNSts); Hydrochloric acid (HCl); Hydrogen tetrachloroaurate (III) hydrate (HAuCl4); Inductively coupled plasma mass spectrometry (ICP-MS); Localized surface plasmon resonance (LSPR); Methotrexate (MTX); N, N, N', N", N"-Pentamethyl diethylenetriamine (PMDETA); Sodium borohydride ($NaBH_4$); Near-infrared (NIR); N-Hydroxysuccinimide (NHS); Photoacoustic tomography (PAT); Photothermal therapy (PTT); Poly (vinyl pyrrolidone) (PVP); Propidium iodide (PI); Proton nuclear magnetic resonance (^1H NMR); Rhodamine B (RhoB); Roswell Park Memorial Institute 1640 growth medium (RPMI); Silver nitrate ($AgNO_3$); Sodium bromide (NaBr); Sodium chloride (NaCl); Sodium sulfide (Na_2S); Tertiary amine (TA); Transmission electron microscopy (TEM); Triethylamine (TEA); X-ray computed tomography (CT)

Declarations

Ethics approval and consent to participate

Not applicable

Consent for publication

Not applicable

Availability of data and materials

Not applicable

Competing interests

The authors declare that they have no competing interests

Funding

This study was financially supported by grant no. 59950 from Faculty of Advanced Medical Science, Tabriz University of Medical Sciences, Tabriz, Iran.

Authors' contributions

M.A done all parts of experiments, data gathering and participate in manuscript writing. A.P synthesis the gold nanostructures and analysis data related to this part. R.R advised in cell culture experiments and participated in manuscript writing examination. F.B set up the PTT tests. H.DM help participate in fluorescent imaging of nanoparticles. H.K performed the Rt-qPCR test and analysis this section data. R.S, H.V and M.M are co-supervisors of the project. R.S designed the project, participated in synthesis of polymers, cell culture experiments, data analysis and manuscript writing. H.V participated in data analysis and manuscript writing. M.M participated in imaging data analysis.

Acknowledgments

This study was financially supported by grant no. 59950 from Faculty of Advanced Medical Science, Tabriz University of Medical Sciences, Tabriz, Iran.

References

1. Beik J, Khateri M, Khosravi Z, Kamrava SK, Kooranifar S, Ghaznavi H, Shakeri-Zadeh A. Gold nanoparticles in combinatorial cancer therapy strategies. Coord Chem Rev. 2019;387:299–324.
2. Bock C, Lengauer T. Managing drug resistance in cancer: lessons from HIV therapy. Nat Rev Cancer. 2012;12(7):494–501.
3. Bouwman P, Jonkers J. The effects of deregulated DNA damage signalling on cancer chemotherapy response and resistance. Nat Rev Cancer. 2012;12(9):587–98.
4. Samson DJ, Seidenfeld J, Ziegler K, Aronson N. Chemotherapy sensitivity and resistance assays: a systematic review. Journal of clinical oncology. 2004;22(17):3618–30.
5. Schroeder A, Heller DA, Winslow MM, Dahlman JE, Pratt GW, Langer R, Jacks T, Anderson DG. Treating metastatic cancer with nanotechnology. Nat Rev Cancer. 2012;12(1):39–50.
6. Yu H, Cui Z, Yu P, Guo C, Feng B, Jiang T, Wang S, Yin Q, Zhong D, Yang X. pH-and NIR light-responsive micelles with hyperthermia-triggered tumor penetration and cytoplasm drug release to reverse doxorubicin resistance in breast cancer. Adv Func Mater. 2015;25(17):2489–500.
7. Rai P, Mallidi S, Zheng X, Rahmanzadeh R, Mir Y, Elrington S, Khurshid A, Hasan T. Development and applications of photo-triggered theranostic agents. Adv Drug Deliv Rev. 2010;62(11):1094–124.
8. MacKay JA, Li Z. (2010) Development of theranostic agents that co-deliver therapeutic and imaging agents. Advanced drug delivery reviews 62 (11).
9. Grassberger C, Paganetti H. Methodologies in the modeling of combined chemo-radiation treatments. Phys Med Biol. 2016;61(21):R344.

10. Zhan Q, Yi K, Qi H, Li S, Li X, Wang Q, Wang Y, Liu C, Qiu M, Yuan X. Engineering blood exosomes for tumor-targeting efficient gene/chemo combination therapy. Theranostics. 2020;10(17):7889.
11. Hu H, Xiao C, Wu H, Li Y, Zhou Q, Tang Y, Yu C, Yang X, Li Z. Nanocolloidosomes with selective drug release for active tumor-targeted imaging-guided photothermal/chemo combination therapy. ACS Appl Mater Interfaces. 2017;9(48):42225–38.
12. Yang HW, Hua MY, Hwang TL, Lin KJ, Huang CY, Tsai RY, Ma CCM, Hsu PH, Wey SP, Hsu PW. Non-invasive synergistic treatment of brain tumors by targeted chemotherapeutic delivery and amplified focused ultrasound-hyperthermia using magnetic nanographene oxide. Advanced materials. 2013;25(26):3605–11.
13. Kim J-W, Galanzha EI, Shashkov EV, Moon H-M, Zharov VP. Golden carbon nanotubes as multimodal photoacoustic and photothermal high-contrast molecular agents. Nature nanotechnology. 2009;4(10):688–94.
14. Zhi D, Yang T, O'hagan J, Zhang S, Donnelly RF. Photothermal therapy. Journal of Controlled Release; 2020.
15. Chen Y, Gao Y, Chen Y, Liu L, Mo A, Peng Q. Nanomaterials-based photothermal therapy and its potentials in antibacterial treatment. Journal of Controlled Release; 2020.
16. Dreaden EC, Alkilany AM, Huang X, Murphy CJ, El-Sayed MA. The golden age: gold nanoparticles for biomedicine. Chem Soc Rev. 2012;41(7):2740–79.
17. Bardhan R, Lal S, Joshi A, Halas NJ. Theranostic nanoshells: from probe design to imaging and treatment of cancer. Acc Chem Res. 2011;44(10):936–46.
18. Xia Y, Li W, Cobley CM, Chen J, Xia X, Zhang Q, Yang M, Cho EC, Brown PK. Gold nanocages: from synthesis to theranostic applications. Acc Chem Res. 2011;44(10):914–24.
19. Srivatsan A, Jenkins SV, Jeon M, Wu Z, Kim C, Chen J, Pandey RK. Gold nanocage-photosensitizer conjugates for dual-modal image-guided enhanced photodynamic therapy. Theranostics. 2014;4(2):163.
20. Azizi M, Valizadeh H, Shahgolzari M, Talebi M, Baybordi E, Dadpour MR, Salehi R, Mehrmohammadi M. Synthesis of Self-Targeted Carbon Dot with Ultrahigh Quantum Yield for Detection and Therapy of Cancer. ACS omega. 2020;5(38):24628–38.
21. Mackey MA, Ali MR, Austin LA, Near RD, El-Sayed MA. The most effective gold nanorod size for plasmonic photothermal therapy: theory and in vitro experiments. J Phys Chem B. 2014;118(5):1319–26.
22. Li Z, Huang H, Tang S, Li Y, Yu X-F, Wang H, Li P, Sun Z, Zhang H, Liu C. Small gold nanorods laden macrophages for enhanced tumor coverage in photothermal therapy. Biomaterials. 2016;74:144–54.
23. Yuan H, Fales AM, Khoury CG, Liu J, Vo-Dinh T. Spectral characterization and intracellular detection of Surface-Enhanced Raman Scattering (SERS)-encoded plasmonic gold nanostars. Journal of Raman spectroscopy. 2013;44(2):234–9.
24. Liu Y, Ashton JR, Moding EJ, Yuan H, Register JK, Fales AM, Choi J, Whitley MJ, Zhao X, Qi Y. A plasmonic gold nanostar theranostic probe for in vivo tumor imaging and photothermal therapy.

Theranostics. 2015;5(9):946.
25. Zhou K, Wang Y, Huang X, Luby-Phelps K, Sumer BD, Gao J. Tunable, ultrasensitive pH-responsive nanoparticles targeting specific endocytic organelles in living cells. Angew Chem Int Ed. 2011;50(27):6109–14.
26. Chen Y-H, Tsai C-Y, Huang P-Y, Chang M-Y, Cheng P-C, Chou C-H, Chen D-H, Wang C-R, Shiau A-L, Wu C-L. Methotrexate conjugated to gold nanoparticles inhibits tumor growth in a syngeneic lung tumor model. Mol Pharm. 2007;4(5):713–22.
27. Dong B, Du S, Wang C, Fu H, Li Q, Xiao N, Yang J, Xue X, Cai W, Liu D. Reversible self-assembly of nanoprobes in live cells for dynamic intracellular pH imaging. ACS Nano. 2019;13(2):1421–32.
28. Espinosa A, Silva AK, Sánchez-Iglesias A, Grzelczak M, Péchoux C, Desboeufs K, Liz-Marzán LM, Wilhelm C. Cancer cell internalization of gold nanostars impacts their photothermal efficiency in vitro and in vivo: toward a plasmonic thermal fingerprint in tumoral environment. Advanced healthcare materials. 2016;5(9):1040–8.
29. Nergiz SZ, Gandra N, Tadepalli S, Singamaneni S. Multifunctional hybrid nanopatches of graphene oxide and gold nanostars for ultraefficient photothermal cancer therapy. ACS Appl Mater Interfaces. 2014;6(18):16395–402.
30. Rahimi M, Safa KD, Alizadeh E, Salehi R. Dendritic chitosan as a magnetic and biocompatible nanocarrier for the simultaneous delivery of doxorubicin and methotrexate to MCF-7 cell line. New J Chem. 2017;41(8):3177–89.
31. Rahmani A, Mousavi HZ, Salehi R, Bagheri A. Novel pH-sensitive and biodegradable micelles for the combined delivery of doxorubicin and conferone to induce apoptosis in MDA-MB-231 breast cancer cell line. RSC Advances. 2020;10(49):29228–46.
32. Sabzi A, Rahmani A, Edalati M, Kahroba H, Dadpour MR, Salehi R, Zarebkohan A. Targeted co-delivery of curcumin and doxorubicin by citric acid functionalized Poly (ε-caprolactone) based micelle in MDA-MB-231 cell. Colloids Surf B. 2020;194:111225.
33. Han J-H, Park J, Kang T-B, Lee K-H. Regulation of Caspase-8 Activity at the Crossroads of Pro-Inflammation and Anti-Inflammation. Int J Mol Sci. 2021;22(7):3318.
34. Li X-D, Liang X-L, Yue X-L, Wang J-R, Li C-H, Deng Z-J, Jing L-J, Lin L, Qu E-Z, Wang S-M. Imaging guided photothermal therapy using iron oxide loaded poly (lactic acid) microcapsules coated with graphene oxide. Journal of Materials Chemistry B. 2014;2(2):217–23.

Figures

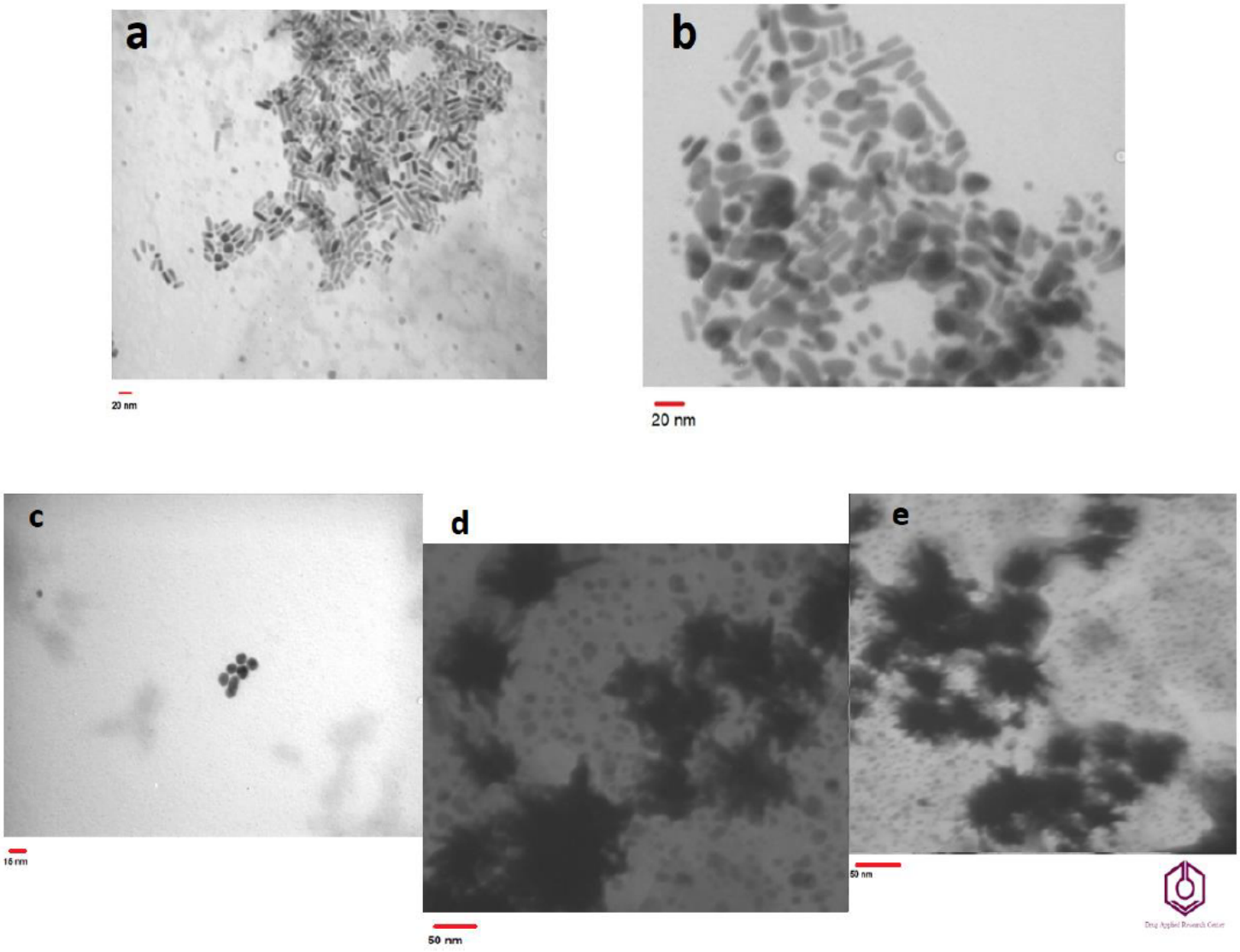

Figure 1

TEM image of synthesized GNSs and Pol-CD@GNSs-MTX. (a) GNRs with an average size of 32± 5.2 nm. (b) Pol-CD@GNRs-MTX with an average size of 39± 4.3 nm. (c) GNSPhs with an average size of 17± 3.2 nm. (d) GNSts with an average size of 43.2 ± 8.2 nm. (e) Pol-CD@GNSts-MTX with an average size of 49.6 ± 7.1 nm.

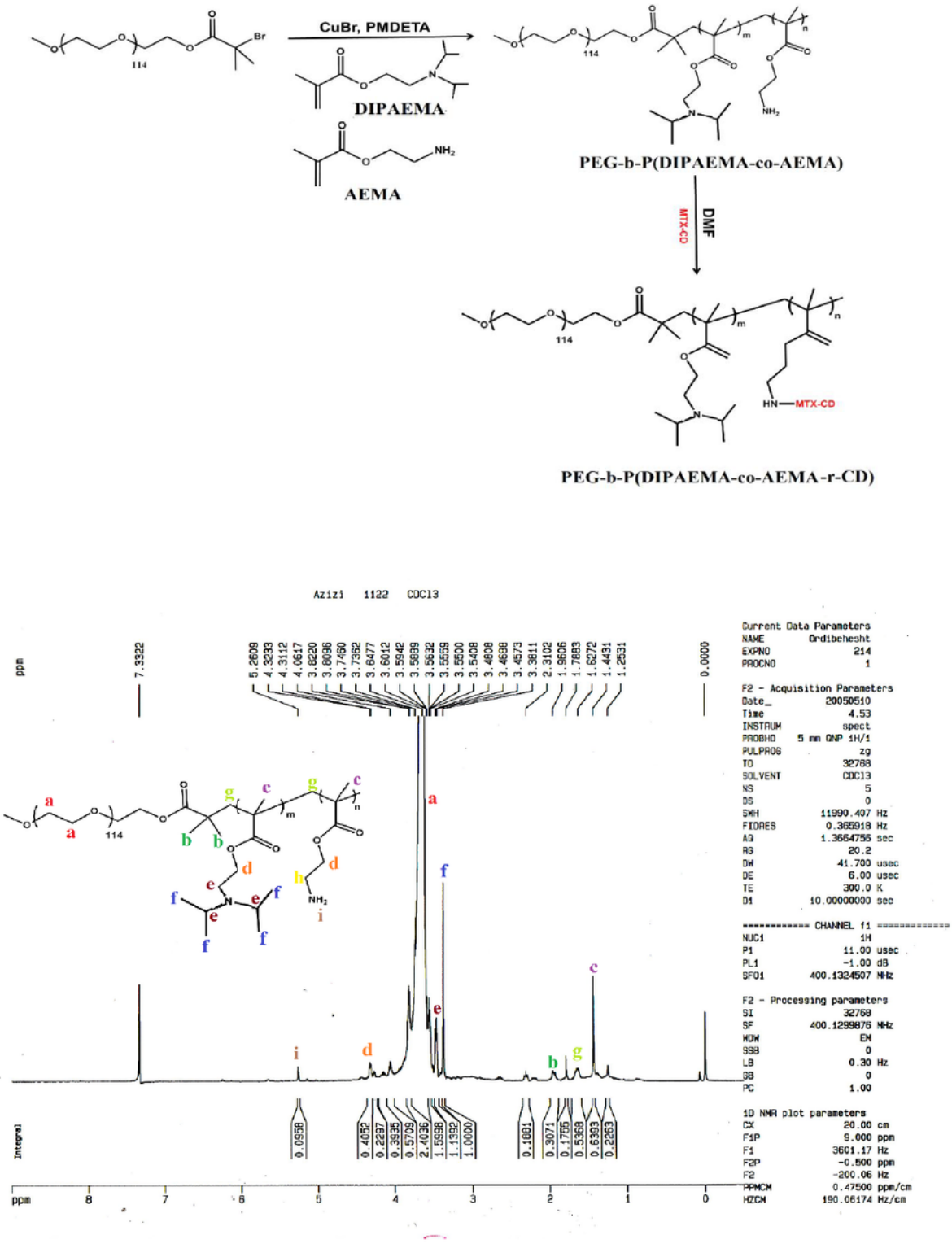

Figure 2

a) Synthetic route of MTX-CD conjugated PEG-b- P(DiPAEMA-co-AEMA). b)1H NMR spectra of PEG-b-P(DiPAEMA-co-AEMA) in CDCl3, 400Hz, ppm)

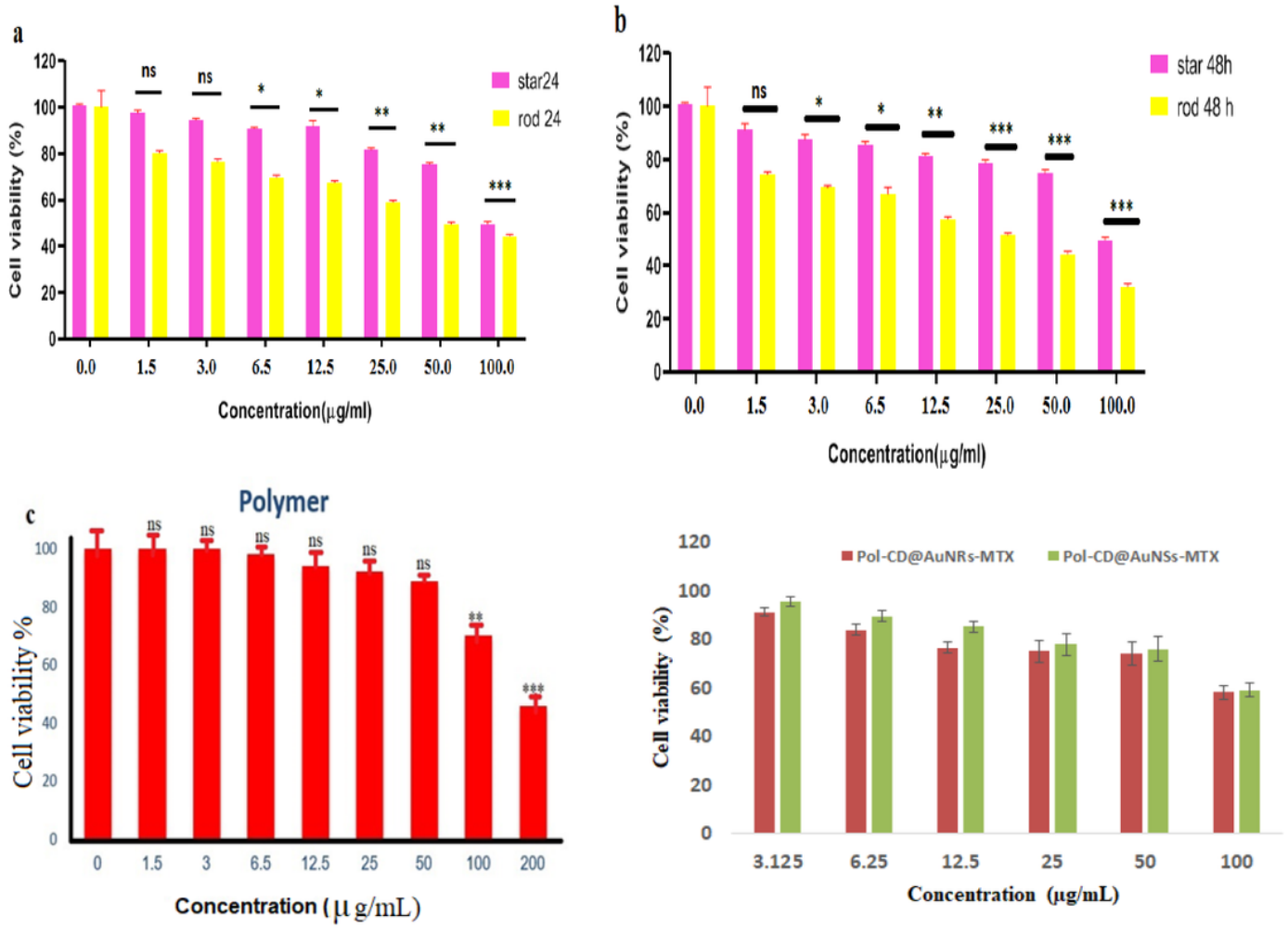

Figure 3

Cell viability of MDA-MB 231 after 24 (a) and 48h (b) incubation with GNRs and GNSts. c) PEG-b-P(DiPAMA-co-AEMA) copolymer, and d) Pol-CD@GNSts-MTX and Pol-CD@GNRs-MTX in different concentrations.

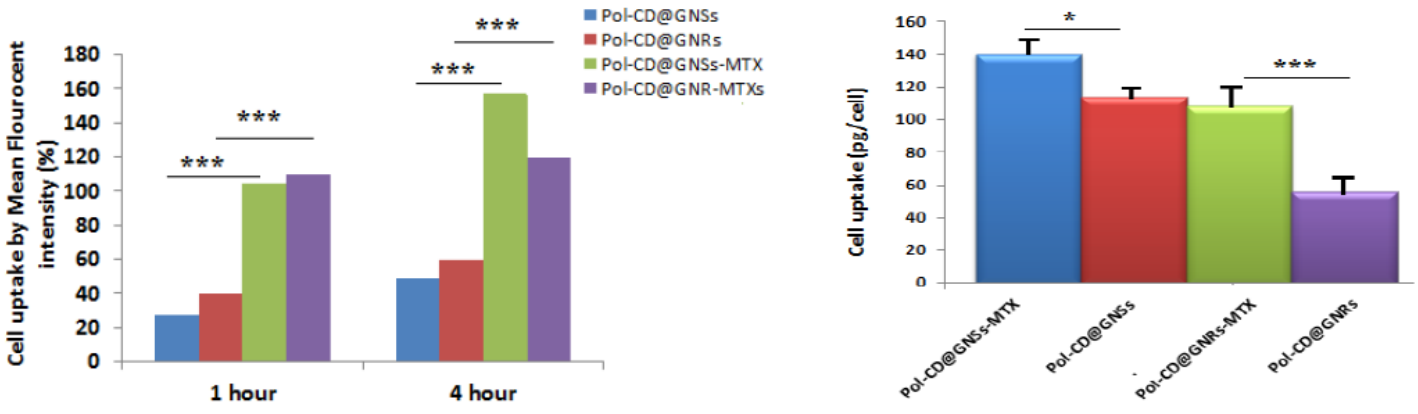

Figure 4

Quantitative cellular uptake analysis: a) Diagram of mean fluorescence intensity (%) of Pol-CD@GNSs and Pol-CD@GNSs-MTX that were uptaken by MDA-MB-231 cells in different time intervals: 1 and 4 h, using flow cytometry; (the differences between treatments was statistically significant, $p < 0.001$); b) ICP-MS (after 4 hours).

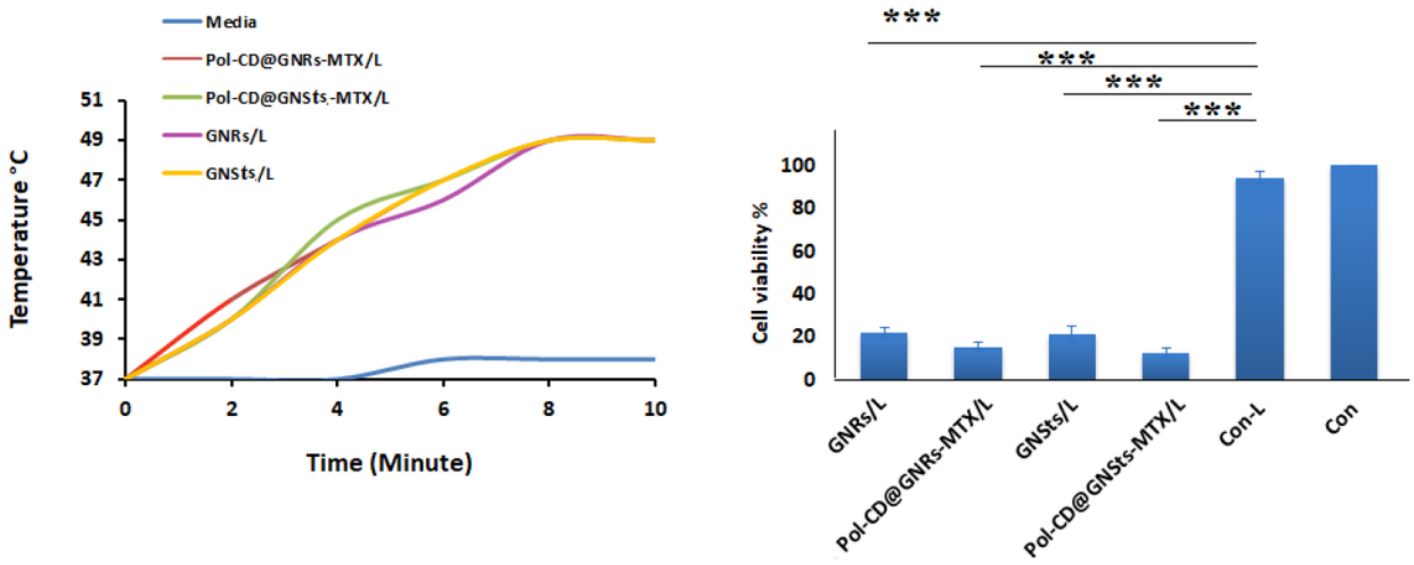

Figure 5

a) The plots of time-dependent temperature increase for suspensions of GNRs(purple), GNSts (sky blue), Pol-CD@GNRs-MTX, Red), Media (blue), and Pol-CD@GNSts-MTX, Green) as a function of irradiation time using an 808 nm laser with the power density of 0.7W/cm2, b). Cell viability of designed GNRs/L, Pol-CD@GNRs-MTX/L, GNSts/L, Pol-CD@GNSts-MTX/L all with the concentration of 50 µg/ml along with laser irradiation.

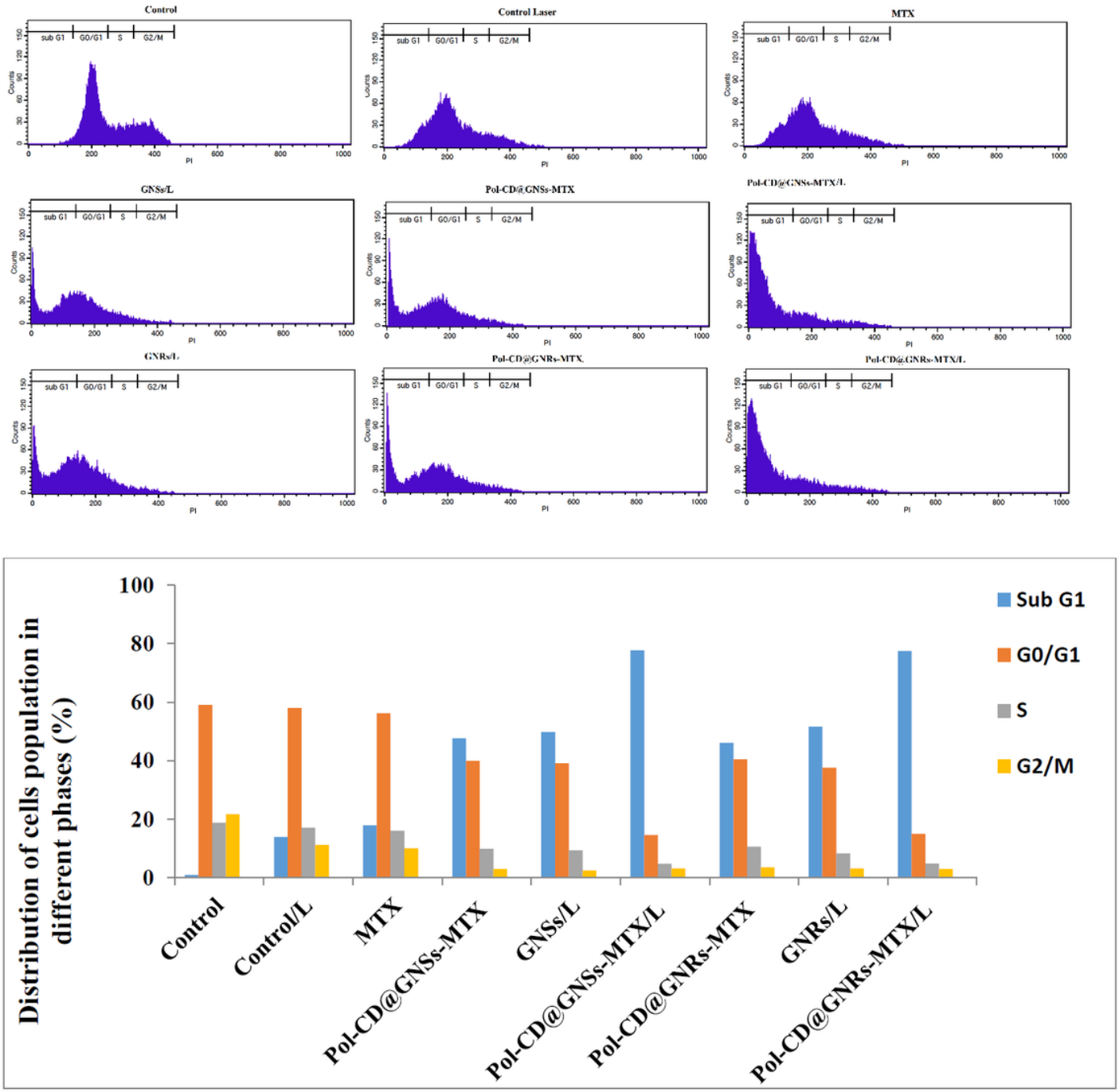

Figure 6

a) Cell cycle arrest analysis using flow cytometry: Effect of Control Laser, MTX, GNRs+Laser, Pol-CD@GNRs-MTX, Pol-CD@GNRs-MTX+Laser, GNSts+Laser, Pol-CD@GNSts-MTX, and Pol-CD@GNSts-MTX+ Laser treatments (48 hours) in the MDA-MB-231 cell cycle. Untreated cells were considered as control. b) Quantitative percentage of MDA-MB 231 distribution in various cell cycle phases after 48 hours.

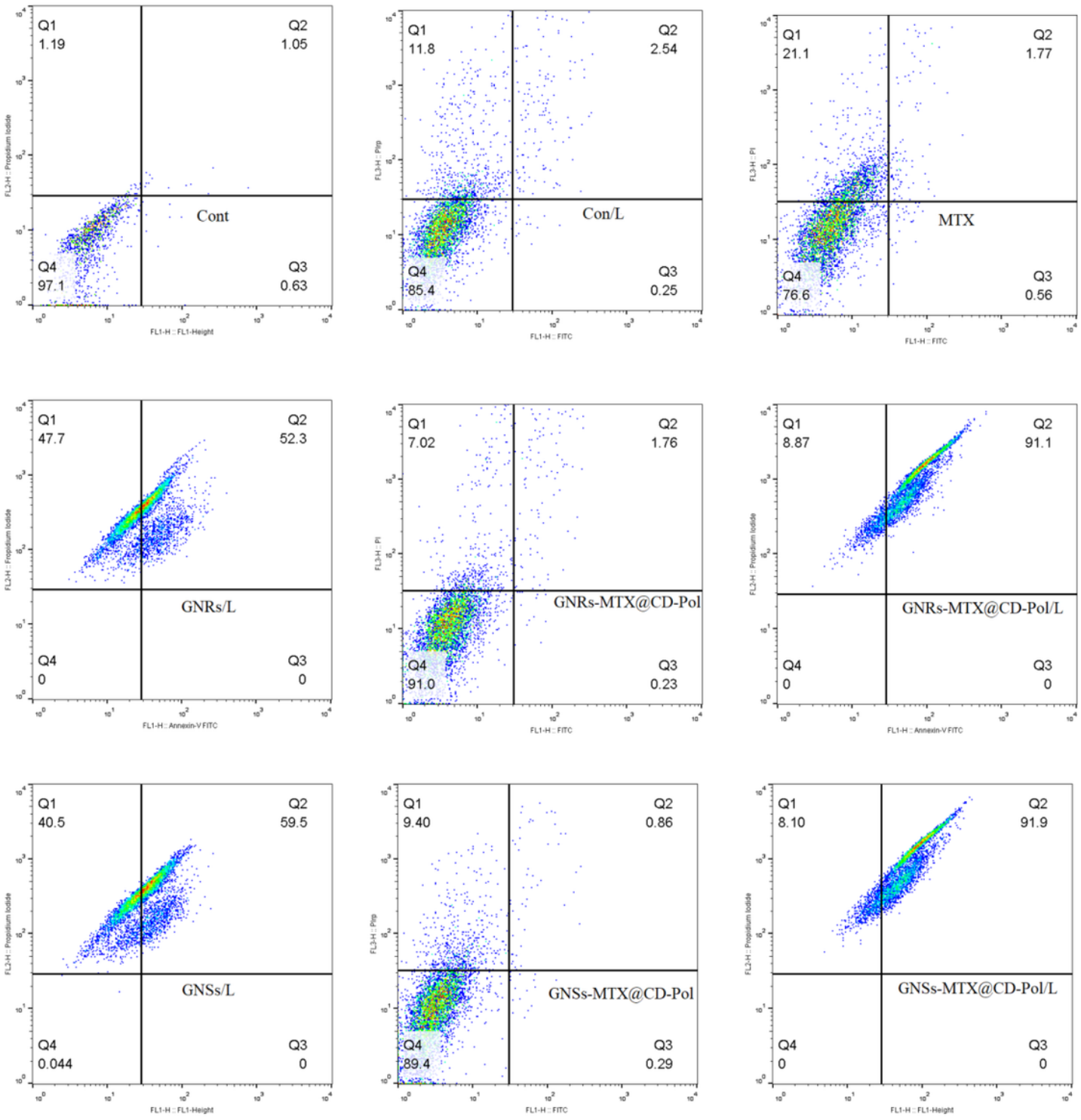

Figure 7

The apoptotic effects of treatments composed of Control Laser, MTX, GNRs+Laser, Pol-CD@GNRs-MTX, Pol-CD@GNRs-MTX+Laser, GNSts+Laser, Pol-CD@GNSts-MTX, and Pol-CD@GNSts-MTX+Laser in MDA-MB-231 cells were determined by flow cytometry. Untreated cells were considered as control.

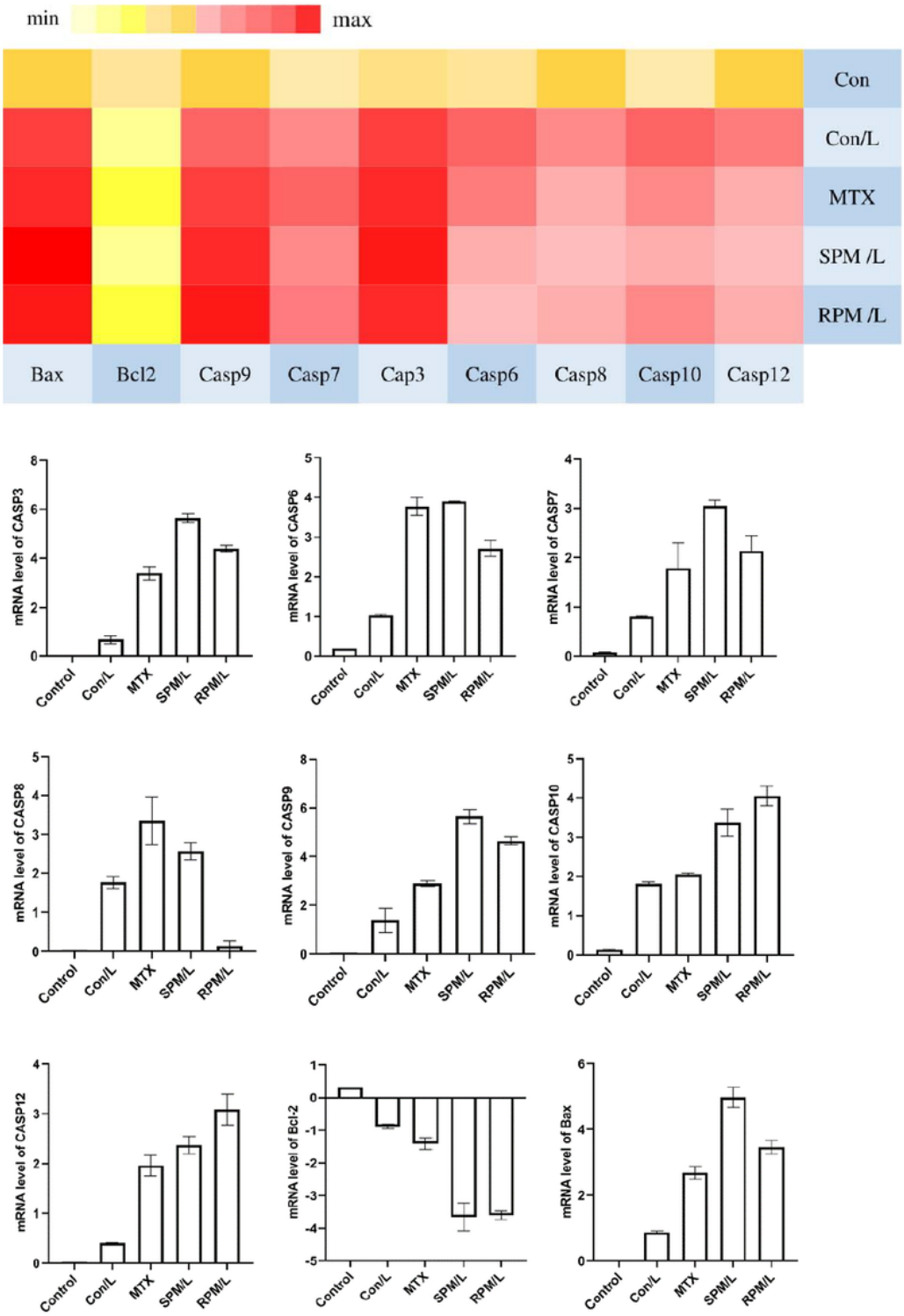

Figure 8

QRT-PCR expressions of apoptosis pathways (a,b). The heat map (a) and graphs (b) depict different ranges of apoptosis pathway expression in in MDA-MB-231 cells treated with Pol-CD@GNRs-MTX+Laser and Pol-CD@GNSts-MTX+Laser, MTX. Cells treated with laser only (808 nm, 0.7 W/cm2, 10 min) were considered as positive control and non-treated cells were considered as negative. Approximately, Bcl2 depicts down-regulation in all samples. Expression of Bax, Caspases 3 and 9 was increased which is in

the benefit of the intrinsic apoptosis pathway. (Con: Control, MTX: Methotrexate, SPM/L: Pol-CD@GNSts-MTX/Laser, RPM/L: Pol-CD@GNRs-MTX/Laser). All treatment groups showed statistically significant differences compared to control matched-control groups (0.05<p value<0.0001)

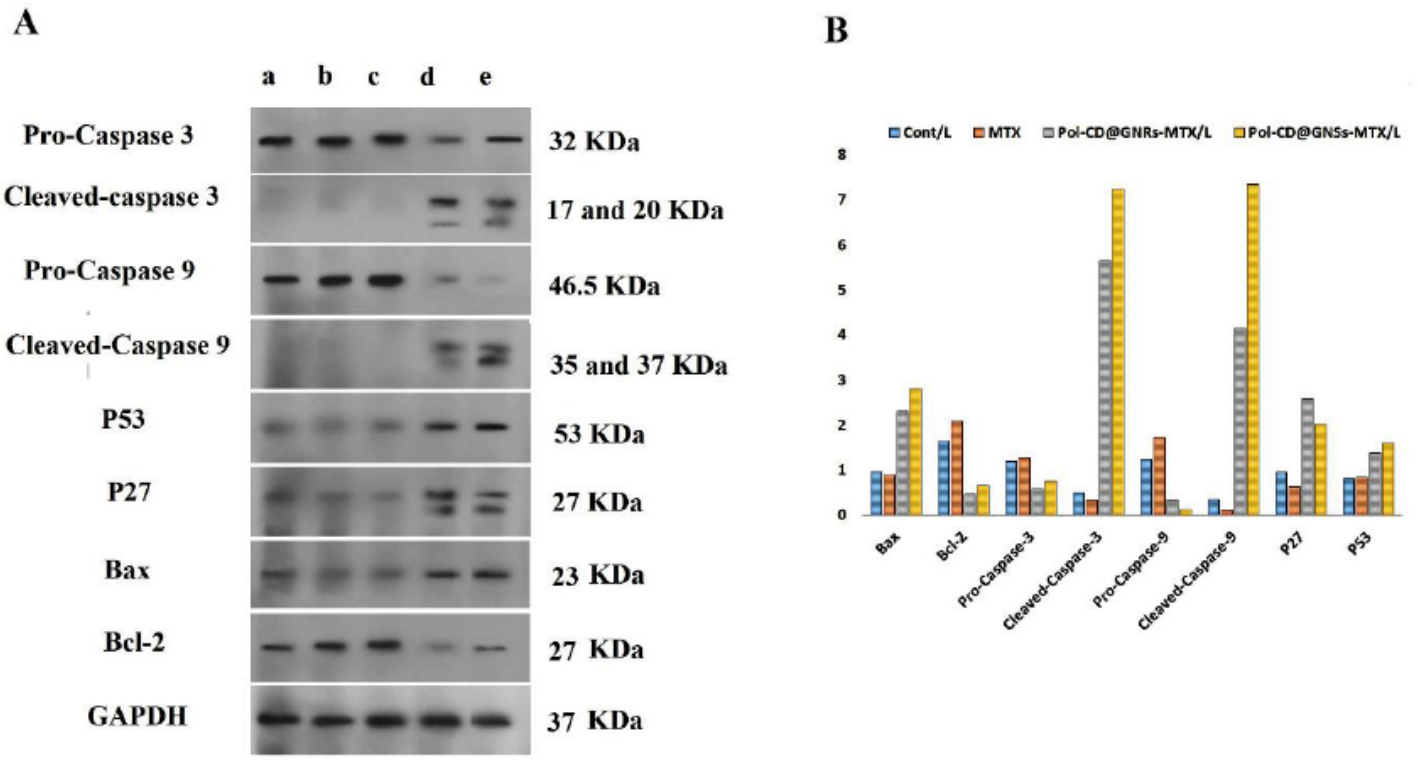

Figure 9

A) Western blot analysis of different proteins (caspase 3, caspase 9, P27, P53, Bax, Bcl2) regulated by a: Control, b: Control laser, c: MTX, d: Pol-CD@GNRs-MTX/L, and e: Pol-CD@GNSts-MTX/L in inducing different apoptotic pathways in MDA-MB 231 cells. GAPDH was considered as a control. B) Quantitative results of apoptotic effects assessed by western blot analysis.

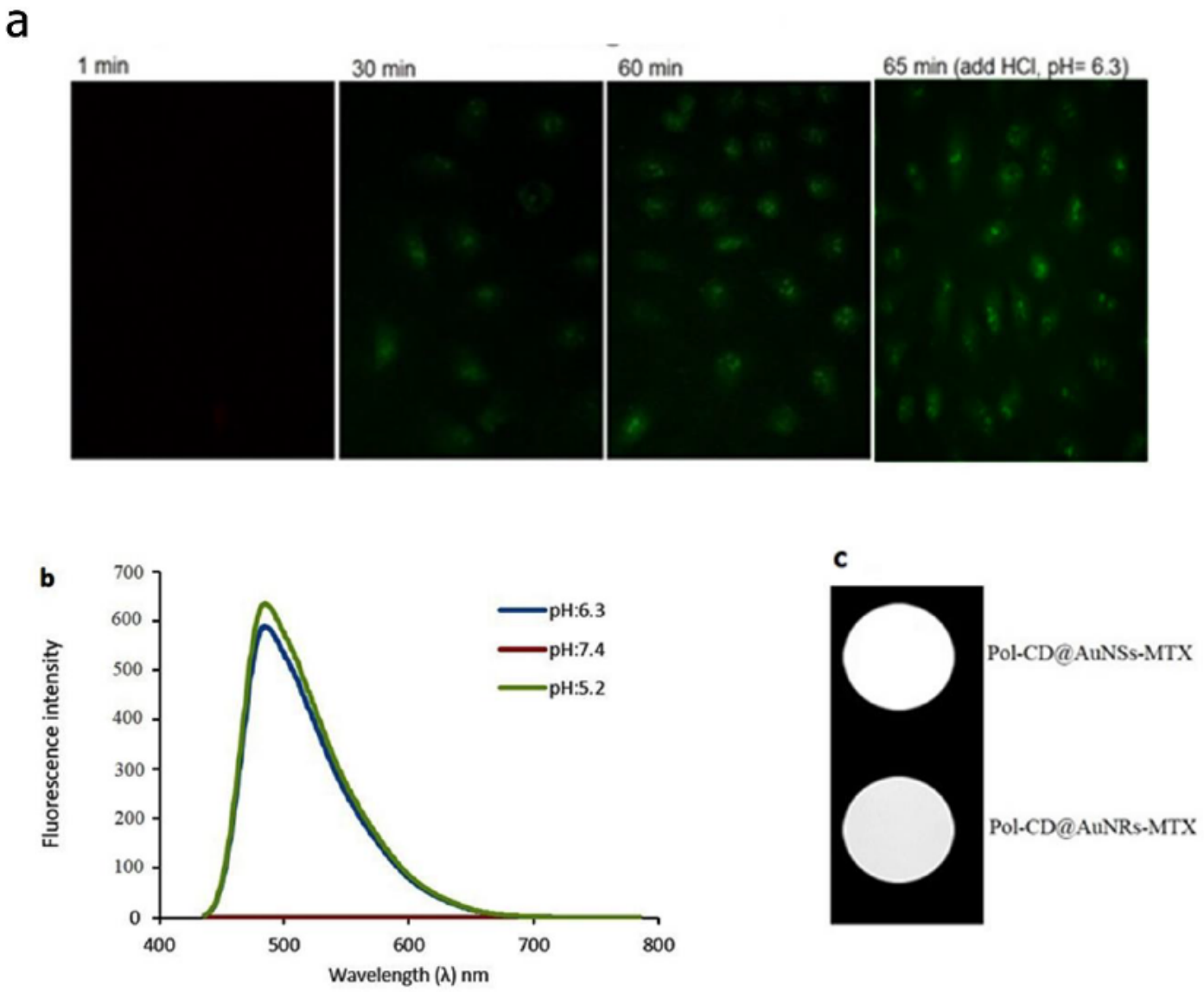

Figure 10

In vitro fluorescence and CT imaging of MDA-MB 231 cells. (a). Representative images of activated Pol-CD@GNSs-MTX (pHt = 6.3 at concentration of 50 μg/mL)) over time. (b). Fluorescence intensity in different pH. (c). CT imaging of Pol-CD@GNSs-MTX (pHt = 6.3). Pol-CD@GNSs-MTX was used at concentration of 50 μg/mL

Supplementary Files

This is a list of supplementary files associated with this preprint. Click to download.

- GraphicalAbstract.tif

- Suplementaryfile.docx